Advances in Nano Research, *Vol. 19, No. 3 (2025) 225-236*
https://doi.org/10.12989/anr.2025.19.3.225

Stability analysis and visual design of carbon nanotube-reinforced spherical shells products using higher-order theories and HDQM

Wu Qiang*[1,2], Ahmad Zuhairi Bin Abdul Majid[2] and Murat Yaylacı[3,4]

[1]*College of Art, Wuyi University, Wuyishan, 354300, China*
[2]*School of Art, University Sains Malaysia, Pulau Pinang, 11800, Malaysia*
[3]*Department of Civil Engineering, Recep Tayyip Erdogan University, 53100, Rize, Turkey*
[4]*Turgut Kıran Maritime Faculty, Recep Tayyip Erdogan University, 53900, Rize, Turkey*

(*Received February 16, 2025, Revised August 23, 2025, Accepted August 25, 2025*)

Abstract. This paper presents an in-depth investigation concerning the stability, temporary position, and visual design of spherical shells having functional graded carbon nanotube (FG-CNT) reinforced composites (FG-CNTRC) is investigated in this study. The analysis is based on Higher-order theories, in particular, the 12-variable displacement field (HOST12), which adequately describes the kinematic behavior of the shell. The material properties of FG-CNTRC were based on the Rule of Mixtures, thus the geometrically and materially nonlinear distribution and interaction of carbon nanotubes with matrix was described and incorporated. The stability of the FG-CNTRC spherical shells are investigated by developing the governing equations of motion via Hamilton's principle, thus accounting for material and geometrical parameters. To discretize the governing equations a hyperbolic differential quadrature method (HDQM) is employed based on Chebyshev–Gauss–Lobatto grid points, ensuring high accuracy and convergence in the results. Complete stability analyses are carried out by varying the effects of the volume fraction of the carbon nanotube and the geometry of the shell for visual design. The results point out the critical buckling loads and two deformation characteristics, along with the improvements in performance for FG-CNTRC shells versus typical materials. The findings are also compared to results reported by other authors in the literature showing the improved accuracy and reliability of the proposed approach. This study both reinforces the move toward sophisticated higher-order theories for the design of nanoreinforced structures and addresses an emerging field of knowledge related to the topic of nanocomposites for use in structural engineering.

Keywords: FG-CNTRC; HDQM; higher-order theories; spherical shells products; stability analysis; visual design

1. Introduction

Composite materials have become an essential part of modern engineering due to their exceptional performance characteristics, including high strength-to-weight ratios, durability, and the ability to tailor properties for specific applications (Beitollahi *et al*. 2025). The versatility of composite structures makes them indispensable in a wide range of industries, from aerospace to civil engineering, automotive, and even energy systems (Gawah *et al*. 2025a). Engineers have increasingly relied on composite materials to design lighter, stronger, and more efficient structures that would be impossible or highly impractical with traditional materials like metals or concrete (Bousmaha *et al*. 2025). The incorporation of fibers, such as carbon nanotubes or glass fibers, into a matrix material allows engineers to achieve superior mechanical properties without significantly increasing the material's weight (Gawah *et al*. 2025b). This results in products that are not only more efficient but also more sustainable, as lighter structures often translate into lower energy consumption during production, transportation, and operation (Gawah *et al*. 2024). The growing demand for high-performance materials in sectors like aerospace has driven significant advancements in composite technology, prompting engineers to develop novel solutions for complex design challenges (Youzera *et al*. 2025). Engineers are particularly interested in composites because they can be tailored for specific environmental conditions (Al-Houri *et al*. 2024a). Whether it's resistance to corrosion, high-temperature stability, or enhanced fatigue resistance, composites can be designed to meet the exact demands of a given application (Tounsi *et al*. 2024). Furthermore, the ability to customize composite materials—through variation in fiber orientation, matrix composition, and volume fractions—has opened new doors for innovative structural designs (Al-Houri *et al*. 2024b). The design of composite structures also presents unique challenges, particularly in the analysis and simulation of their behavior under different loading conditions (Zerrouki *et al*. 2024). Engineers must consider factors such as interfacial bonding, anisotropy, and the influence of manufacturing processes (Belabed 2024). Understanding these complexities requires advanced analytical methods, including finite element modeling and hybrid displacement methods, which have been increasingly used to improve the accuracy of stability and strength predictions for composite structures (Alsubaie *et al*. 2024). Moreover, the growing integration of nanotechnology has further expanded the potential of composites (Alsubaie *et al*. 2023). By incorporating nanoparticles, such as carbon

*Corresponding author, Ph.D.,
E-mail: wqcpsj@wuyiu.edu.cn

ISSN: 2287-237X (Print), 2287-2388 (Online)

nanotubes, into composite materials, engineers can significantly enhance their mechanical properties, electrical conductivity, and thermal resistance (Safarpour *et al*. 2021). As technology progresses, engineers are continually finding new ways to leverage composite materials for innovative applications, highlighting their growing importance in modern engineering design (SafarPour *et al*. 2019). Ultimately, composites have revolutionized the way engineers approach material selection and structural design (Ayache *et al*. 2018). With ongoing research into optimizing composite structures, engineers are better equipped to meet the evolving demands of performance, sustainability, and cost-effectiveness across a variety of industries (Safarpour *et al*. 2025).

Stability analysis is crucial for engineers because it ensures that structures can withstand external forces without experiencing failure or unexpected deformations (Samaniego *et al*. 2020). By assessing stability, engineers can identify critical points where structures may buckle, collapse, or undergo instability under different loading conditions (Zhuang *et al*. 2021). This analysis is particularly important for ensuring the safety and longevity of buildings, bridges, aircraft, and other critical infrastructure (Guo *et al*. 2021). Stability analysis helps engineers optimize material use, ensuring that structures are both safe and cost-effective without overdesigning (Bie *et al*. 2024). In dynamic systems, stability analysis allows engineers to predict how structures will respond to vibrations, seismic activity, or wind forces, preventing catastrophic failures (Liu *et al*. 2024). It also aids in the design of systems that can tolerate unpredictable environmental factors, such as temperature fluctuations or impact forces (Avcar *et al*. 2023). Without proper stability assessments, engineers risk designing structures that may fail under normal operating conditions, leading to costly repairs or accidents (Shen *et al*. 2024). Moreover, stability analysis supports the development of more efficient and innovative designs, as engineers can push the limits of material properties and structural configurations with confidence (Djebbour *et al*. 2025). As engineering designs become increasingly complex and materials more advanced, stability analysis becomes even more critical in ensuring performance under real-world conditions (Hajmohammad *et al*. 2018). Therefore, stability analysis is not only a safety measure but also a tool that enables engineers to create resilient, high-performing structures (Kumar *et al*. 2021).

This study investigates the stability and design optimization of spherical shells reinforced with FG-CNTRC, employing higher-order theories. A 12-variable displacement field is utilized to capture the shell's kinematic behavior with high accuracy. Material properties are modeled based on the Rule of Mixtures to reflect the distribution of carbon nanotubes within the composite matrix. The stability analysis is derived using Hamilton's principle, incorporating both geometric and material linearity. To solve the governing equations efficiently, HDQM based on Chebyshev–Gauss–Lobatto grid points is implemented. The results reveal the influence of key parameters, such as the nanotube volume fraction, on the buckling load and deformation characteristics of the shell.

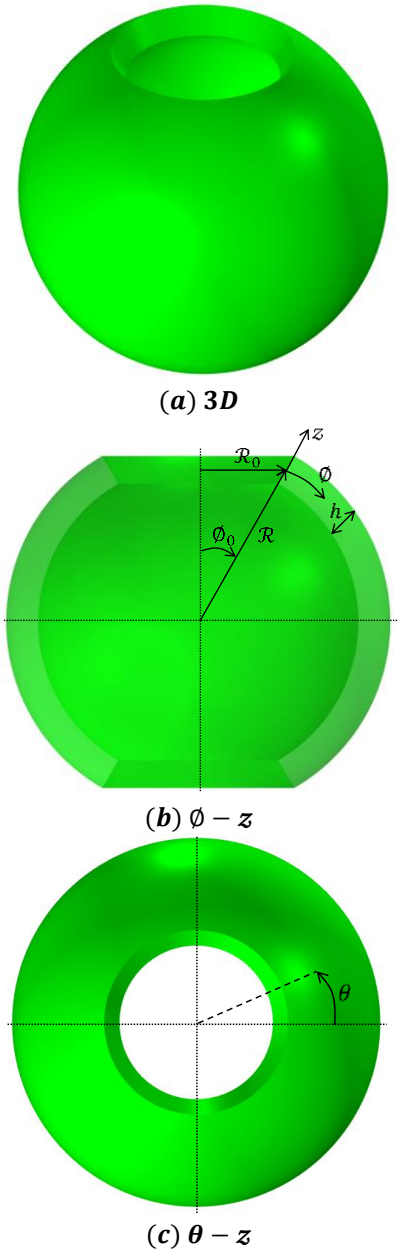

$(\boldsymbol{a})$ $\boldsymbol{3D}$ $(\boldsymbol{b})$ $\boldsymbol{\emptyset - z}$ $(\boldsymbol{c})$ $\boldsymbol{\theta - z}$

Fig. 1 A spherical shell with different views

By comparing the current results with those of previous studies, a marked improvement in accuracy is observed, particularly in predicting critical stability thresholds. This work provides a robust framework for the design and optimization of advanced nanoreinforced composite structures, offering insights for future applications in engineering fields requiring lightweight, high-strength materials.

2. Basic equation

Fig. 1 depicts a spherical shell with different views: 3D (a), $\emptyset - z$ (b), and $\theta - z$ (c). In the 3D view (a), the shell is shown in its entirety, illustrating its spherical shape. The $\emptyset - z$ view (b) focuses on the radial ($\mathcal{R}_o$) and angular (ϕ_0)

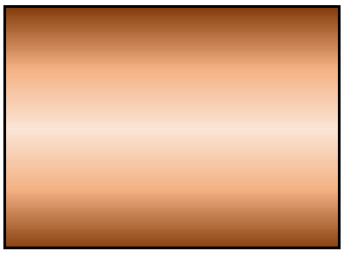

$(\boldsymbol{a})\ \boldsymbol{FG-X}$

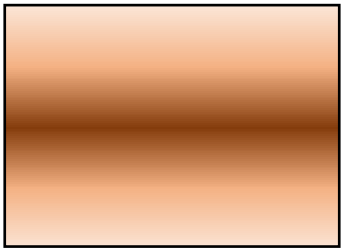

$(\boldsymbol{b})\ \boldsymbol{FG-O}$

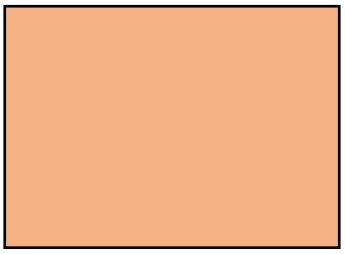

$(\boldsymbol{c})\ \boldsymbol{FG-UD}$

Fig. 2 Three various dispersions of CNTs along with the thickness of the spherical shell

dimensions along with the height (h) and radius $(\mathcal{R})$ parameters, providing a cross-sectional view. The $\theta-z$ view (c) presents a vertical cut through the shell, emphasizing the relationship between the angular and vertical axes. These perspectives are crucial for understanding the shell's geometric properties. The parameters $\mathcal{R}_o$, $\mathcal{R}$, h, and ϕ_0 describe the shell's physical dimensions, including the radius, height, and angular variations. The illustration provides a clear representation of the spherical shell's structure, aiding in its stability analysis, especially in relation to the distribution of material and deformation behavior in spherical coordinate systems. This type of modeling is essential for the design and analysis of advanced composite materials like FG-CNTRC (functionally graded carbon nanotube-reinforced composites). By understanding these geometric parameters and their interactions, researchers can better predict the shell's performance under various loading conditions and optimize its design for engineering applications.

2.1 Mechanical properties of the FG-CNTRC spherical shell

Fig. 2 shows three different patterns for the distribution of carbon nanotubes within a composite material, typically used in functionally graded carbon nanotube-reinforced composites. Here's an explanation of each pattern:

1. (a) FG-X: This pattern represents a gradient in the material where the carbon nanotubes are distributed in the z-direction (likely along the length of the material). The CNTs are arranged in such a way that their concentration increases or decreases across the material, affecting its mechanical properties along the direction of the z -axis.
2. (b) FG-O: In this pattern, the distribution of CNTs follows a circular or radial gradient (denoted by "O"). The material likely has a uniform gradient in terms of the carbon nanotube content, gradually changing in a circular fashion across the cross-section.
3. (c) FG-UD: This stands for uniform distribution (UD) of CNT. In this case, the carbon nanotubes are oriented in a single direction, possibly along the primary axis of the composite (typically the length or depth of the material), providing strength and properties tailored to that specific direction.

These different CNT distribution patterns help enhance various properties of the composite, such as stiffness, strength, and thermal conductivity, by tailoring the material's characteristics in specific directions.

In the presented model, three distinct approaches are proposed to simulate the distribution of single-walled carbon nanotubes (SWCNTs) throughout the thickness of the structure. The calculation of the effective thermo-mechanical properties for the FG-SWCNT reinforced nanocomposite material is carried out using formulations derived from the well-established rule of mixtures (ROM), while also incorporating the efficiency factor associated with SWCNTs (Safarpour and Alibeigloo 2021).

$$E_{11}=\eta_1 V_{\mathrm{CNT}} E_{11}^{\mathrm{CNT}}+\mathrm{V_m} E^{\mathrm{m}}, \tag{1a}$$

$$\frac{\eta_{2\mathrm{U}}}{E_{22\mathrm{U}}}=\frac{V_{\mathrm{CNTU}}}{E_{22}^{\mathrm{CNTU}}}+\frac{V_{\mathrm{m}}}{E^{m}}, \tag{1b}$$

$$\frac{\eta_3}{G_{12}}=\frac{V_{\mathrm{CNT}}}{G_{12}^{\mathrm{CNT}}}+\frac{V_{\mathrm{mU}}}{G^{\mathrm{mU}}}, \tag{1c}$$

$$\nu_{12}=\mathrm{V}_{\mathrm{CNT}}^{*}\nu_{12}^{\mathrm{CNT}}+\mathrm{V_{mU}}\nu^{\mathrm{m}}, \tag{1d}$$

$$\rho=\mathrm{V_{CNT}}\rho^{\mathrm{CNT}}+\mathrm{V_m}\rho^{\mathrm{m}}, \tag{1e}$$

The following equation will be formulated to relate V_m and V_{CNT} as described in Ref. (Liu *et al.* 2021).

$$V_{\mathrm{CNT}}+\mathrm{V_m}=1 \tag{2}$$

To mathematically represent the volume fraction of each dispersion paradigm of SWCNT throughout the thickness of the structure, the following formulations are provided as (Safarpour and Alibeigloo 2021).

$$\begin{gathered}\text{FG-X: } \mathrm{V_{CNT}}=4\mathrm{V_{CNT}^{*}}\left|\frac{z}{h}\right|,\\ \text{FG-O: } \mathrm{V_{GPL}}=2\mathrm{V_{CNT}^{*}}\left(1-2\left|\frac{z}{h}\right|\right),\\ \text{FG-UD: } \mathrm{V_{GPL}}=\mathrm{V_{CNT}^{*}}\end{gathered} \tag{3}$$

V_{CNT}^{*} can be declared by an explicit relation as

$$V_{\mathrm{CNT}}^{*}=\frac{W_{\mathrm{CNT}}}{W_{\mathrm{CNT}}+(\frac{\rho^{\mathrm{CNT}}}{\rho^{\mathrm{M}}})(1\text{-}\mathrm{W_{CNT}})} \tag{4}$$

here, W_{CNT} denotes the weight content of SWCNT.

The following expression describes the relation between other thermomechanical properties of the nanocomposite structure.

$$\begin{gathered} \mathrm{E}_{33}=\mathrm{E}_{22},\ \nu_{21}=\frac{\mathrm{E}_{22}}{\mathrm{E}_{11}}\nu_{12},\ \mathrm{G}_{12}=\mathrm{G}_{13}=\mathrm{G}_{23}, \\ \nu_{13}=\nu_{12},\ \nu_{31}=\nu_{21},\ \nu_{32}=\nu_{23}=\nu_{21} \end{gathered} \tag{5}$$

The material properties of the spherical shells used here are taken from (Safarpour and Alibeigloo 2021).

3. Displacement field

In this study, the 12-variable displacement field (HOST12) is utilized as the displacement field. This formulation offers improved kinematic behavior compared to the first-order shear deformation and classical laminate theories. As a result, shear correction factors are not necessary, and the theory provides more precise interlaminar stress distributions. By expanding the displacements to include the cubic term in the thickness coordinate, the following equation is derived as (Khalili *et al*. 2011).

$$\begin{gathered} \mathcal{U}(\phi,\theta,z,t)=\mathcal{U}_0(\phi,\theta,t)+z\mathcal{U}_1(\phi,\theta,t)+ \\ z^2\mathcal{U}_2(\phi,\theta,t)+z^3\mathcal{U}_3(\phi,\theta,t), \end{gathered} \tag{6a}$$

$$\begin{gathered} \mathcal{V}(\phi,\theta,z,t)=\mathcal{V}_0(\phi,\theta,t)+z\mathcal{V}_1(\phi,\theta,t)+ \\ z^2\mathcal{V}_2(\phi,\theta,t)+z^3\mathcal{V}_3(\phi,\theta,t), \end{gathered} \tag{6b}$$

$$\begin{gathered} \mathcal{W}(\phi,\theta,z,t)=\mathcal{W}_0(\phi,\theta,t)+z\mathcal{W}_1(\phi,\theta,t)+ \\ z^2\mathcal{W}_2(\phi,\theta,t)+z^3\mathcal{W}_3(\phi,\theta,t). \end{gathered} \tag{6c}$$

where $\mathcal{U}$, $\mathcal{V}$, and $\mathcal{W}$ are the displacements in the ϕ-, θ-, and z-directions, respectively. $\mathcal{U}_0$, $\mathcal{U}_1$, $\mathcal{U}_2$, $\mathcal{U}_3$, $\mathcal{V}_0$, $\mathcal{V}_1$, $\mathcal{V}_2$, $\mathcal{V}_3$, $\mathcal{W}_0$, $\mathcal{W}_1$, $\mathcal{W}_2$, and $\mathcal{W}_3$ are functions to be determined.

3.1 Strains

Where strain displacement can be defined as follows

$$\begin{gathered} \mathcal{E}_{\phi\phi}=\frac{\partial\mathcal{U}}{\mathcal{R}\partial\phi}+\frac{\mathcal{W}}{\mathcal{R}},\ \mathcal{E}_{\theta\theta}=\frac{\partial\mathcal{V}}{\mathcal{R}_1\partial\theta}+\frac{\mathcal{U}}{\mathcal{R}\mathcal{R}_1}\frac{\partial\mathcal{R}_1}{\partial\phi}+\frac{\mathcal{W}}{\mathcal{R}}, \\ \mathcal{E}_{zz}=\frac{\partial\mathcal{W}}{\partial z},\ \gamma_{\phi\theta}=\frac{\partial\mathcal{V}}{\mathcal{R}\partial\phi}-\frac{\mathcal{V}}{\mathcal{R}\mathcal{R}_1}\frac{\partial\mathcal{R}_1}{\partial\phi}+\frac{\partial\mathcal{U}}{\mathcal{R}_1\partial\theta}, \\ \gamma_{\phi z}=\frac{\partial\mathcal{U}}{\partial Z}-\frac{\mathcal{U}}{\mathcal{R}}+\frac{\partial\mathcal{W}}{\mathcal{R}\partial\phi},\gamma_{\theta z}=\frac{\partial\mathcal{V}}{\partial z}-\frac{\mathcal{V}}{\mathcal{R}}+\frac{\partial\mathcal{W}}{\mathcal{R}_1\partial\theta}. \end{gathered} \tag{7}$$

By substituting $\mathcal{R}_1=\mathcal{R}\sin\emptyset$ in Eq. (7)

$$\begin{gathered} \mathcal{E}_{\phi\phi}=\frac{\partial\mathcal{U}}{\mathcal{R}\partial\phi}+\frac{\mathcal{W}}{\mathcal{R}},\ \mathcal{E}_{\theta\theta}=\frac{1}{\mathcal{R}\,sin(\phi)}\frac{\partial\mathcal{V}}{\partial\theta}+\frac{cot(\phi)\mathcal{U}}{\mathcal{R}}+\frac{\mathcal{W}}{\mathcal{R}}, \\ \mathcal{E}_{zz}=\frac{\partial\mathcal{W}}{\partial z},\ \gamma_{\phi\theta}=\frac{\partial\mathcal{V}}{\mathcal{R}\partial\phi}-\frac{cot(\phi)\mathcal{V}}{\mathcal{R}}+\frac{1}{\mathcal{R}\,sin(\phi)}\frac{\partial\mathcal{U}}{\partial\theta}, \\ \gamma_{\phi z}=\frac{\partial\mathcal{U}}{\partial z}-\frac{\mathcal{U}}{\mathcal{R}}+\frac{\partial\mathcal{W}}{\mathcal{R}\partial\phi}, \end{gathered} \tag{8}$$

3.2 Stress–strain relations

When $\mathcal{E}_{zz}\neq 0$, indicating that thickness stretching is allowed, the three-dimensional model is applied. For functionally graded materials, the constitutive equations can be written as follows:

$$\begin{Bmatrix}\sigma_{\phi\phi}\\ \sigma_{\theta\theta}\\ \sigma_{zz}\\ \sigma_{\theta z}\\ \sigma_{\phi z}\\ \sigma_{\phi\theta}\end{Bmatrix}=\begin{bmatrix}\mathfrak{T}_{11}&\mathfrak{T}_{12}&\mathfrak{T}_{13}&0&0&0\\ \mathfrak{T}_{12}&\mathfrak{T}_{22}&\mathfrak{T}_{23}&0&0&0\\ \mathfrak{T}_{13}&\mathfrak{T}_{23}&\mathfrak{T}_{33}&0&0&0\\ 0&0&0&\mathfrak{T}_{44}&0&0\\ 0&0&0&0&\mathfrak{T}_{55}&0\\ 0&0&0&0&0&\mathfrak{T}_{66}\end{bmatrix}\begin{Bmatrix}\mathcal{E}_{\phi\phi}\\ \mathcal{E}_{\theta\theta}\\ \mathcal{E}_{zz}\\ \gamma_{\theta z}\\ \gamma_{\phi z}\\ \gamma_{\phi\theta}\end{Bmatrix} \tag{9}$$

The terms involved in Eq. (12) would be obtained as:

$$\mathfrak{T}_{11}=\frac{E_{11}(1-\nu_{23}\nu_{32})}{\Lambda},\quad \mathfrak{T}_{12}=\frac{E_{11}(\nu_{21}+\nu_{31}\nu_{23})}{\Lambda}, \tag{10a}$$

$$\mathfrak{T}_{13}=\frac{E_{11}(\nu_{31}+\nu_{21}\nu_{32})}{\Lambda},\ \mathfrak{T}_{22}=\frac{E_{22}(1-\nu_{13}\nu_{31})}{\Lambda}, \tag{10b}$$

$$\mathfrak{T}_{23}=\frac{E_{22}(\nu_{32}+\nu_{12}\nu_{31})}{\Lambda},\ \mathfrak{T}_{33}=\frac{E_{33}(1-\nu_{12}\nu_{21})}{\Lambda}, \tag{10c}$$

$$\mathfrak{T}_{44}=\mathrm{G}_{23},\ \mathfrak{T}_{55}=\mathrm{G}_{13},\ \mathfrak{T}_{66}=\mathrm{G}_{12}, \tag{10d}$$

$$\Lambda=(1-\nu_{12}\nu_{21}-\nu_{23}\nu_{32}-\nu_{13}\nu_{31}-2\nu_{12}\nu_{23}\nu_{31}). \tag{10e}$$

3.3 Governing equations and boundary conditions

The equations that determine motion are derived based on Hamilton's principle.

$$\delta\int_{t_1}^{t_2}\left(\Pi_k-(\Pi_e+\Pi_{\mathcal{W}})\right)dt=0 \tag{11}$$

Where Π_k, Π_e, and $\Pi_{\mathcal{W}}$ stand for the kinetic energy, potential energy, and work done by the internal load of the system, respectively. Taking the first variation of the strain energy yields

$$\begin{gathered} \delta\Pi_e \\ =\int_{\Omega_0}\left\{\int_{-h/2}^{h/2}\begin{bmatrix}\sigma_{\phi\phi}\delta\mathcal{E}_{\phi\phi}+\sigma_{\theta\theta}\delta\mathcal{E}_{\theta\theta}\\ +\sigma_{\theta\theta}\delta\mathcal{E}_{zz}+\sigma_{\phi\theta}\delta\gamma_{\phi\theta}\\ +\sigma_{\phi z}\delta\gamma_{\phi z}+\sigma_{\theta z}\delta\gamma_{\theta z}\end{bmatrix}dz\right\}\mathcal{R}_1 d\phi d\theta \end{gathered} \tag{12}$$

where Ω_0 is the integration domain in plane (ϕ,θ).

The variation of the kinetic energy is given as:

$$\begin{gathered} \delta\Pi_k=\int_{\Omega_0}\left\{\int_{-h/2}^{h/2}\rho(\ddot{\mathcal{U}}\delta\mathcal{U}+\ddot{\mathcal{V}}\delta\mathcal{V}\right. \\ \left.+\ddot{\mathcal{W}}\delta\mathcal{W})dz\right\}\mathcal{R}_1 d\phi d\theta \end{gathered} \tag{13}$$

The work done by the system:

$$\begin{gathered} \Pi_{\mathcal{W}}=\int_A\frac{P}{2}\left\{\left\{\frac{1}{(\mathcal{R}^2\,sin(\phi)}\frac{\partial}{\partial\phi}\left(sin(\phi)\frac{\partial\mathcal{W}}{\partial\phi}\right)\right\}\right. \\ \left.+\frac{1}{\mathcal{R}^2\,sin^2(\phi)}\frac{\partial^2\mathcal{W}}{\partial\theta^2}\right\}\mathcal{W}dA \end{gathered} \tag{14}$$

where P indicates the In-plane mechanical loading. By substituting Π_e, $\delta\Pi_k$, and $\delta\Pi_{\mathcal{W}}$ into Eq. (11), and then performing the integration through the thickness, followed by integration by parts with respect to ϕ and θ, and

collecting the coefficients of $\delta\,\delta\mathcal{U}_0$, $\delta\mathcal{U}_1$, $\delta\mathcal{U}_2$, $\delta\mathcal{U}_3$, $\delta\mathcal{V}_0$, $\delta\mathcal{V}_1$, $\delta\mathcal{V}_2$, $\delta\mathcal{V}_3$, $\delta\mathcal{W}_0$, $\delta\mathcal{W}_1$, $\delta\mathcal{W}_2$, $\delta\mathcal{W}_3$, the following governing equations are derived:

$$\delta\mathcal{U}_0: \frac{1}{\mathcal{R}}\frac{\partial \mathfrak{n}_{\phi\phi}}{\partial\phi}+\frac{cot(\phi)}{\mathcal{R}}\left(\mathfrak{n}_{\phi\phi}-\mathfrak{n}_{\theta\theta}\right)+\frac{1}{\mathcal{R}\,sin(\phi)}\frac{\partial \mathfrak{n}_{\phi\theta}}{\partial\theta}+\frac{\mathfrak{n}_{\phi z}}{\mathcal{R}}=\mathcal{G}_0\frac{\partial^2\mathcal{U}_0}{\partial t^2}+\mathcal{G}_1\frac{\partial^2\mathcal{U}_1}{\partial t^2}+\mathcal{G}_2\frac{\partial^2\mathcal{U}_2}{\partial t^2}+\mathcal{G}_3\frac{\partial^2\mathcal{U}_3}{\partial t^2}, \tag{15a}$$

$$\delta\mathcal{V}_0: \frac{1}{\mathcal{R}\,sin(\phi)}\frac{\partial \mathfrak{n}_{\theta\theta}}{\partial\theta}+\frac{1}{\mathcal{R}}\frac{\partial \mathfrak{n}_{\phi\theta}}{\partial\phi}+\frac{2\,cot(\phi)}{\mathcal{R}}\mathfrak{n}_{\phi\theta}+\frac{\mathfrak{n}_{\theta z}}{\mathcal{R}}=\mathcal{G}_0\frac{\partial^2\mathcal{V}_0}{\partial t^2}+\mathcal{G}_1\frac{\partial^2\mathcal{V}_1}{\partial t^2}+\mathcal{G}_2\frac{\partial^2\mathcal{V}_2}{\partial t^2}+\mathcal{G}_3\frac{\partial^2\mathcal{V}_3}{\partial t^2}, \tag{15b}$$

$$\delta\mathcal{W}_0: \frac{1}{\mathcal{R}}\frac{\partial \mathfrak{n}_{\phi z}}{\partial\phi}+\frac{1}{\mathcal{R}\,sin(\phi)}\frac{\partial \mathfrak{n}_{\theta z}}{\partial\theta}+\frac{cot(\phi)}{\mathcal{R}}\mathfrak{n}_{\phi z}-\frac{\mathfrak{n}_{\phi\phi}+\mathfrak{n}_{\theta\theta}}{\mathcal{R}}-\left\{\frac{P}{\mathcal{R}^2\,sin(\phi)}\frac{\partial}{\partial\phi}\left(sin(\phi)\frac{\partial\left(W_0+\left(\frac{h}{2}\right)W_1+\left(\frac{h}{2}\right)^2W_2+\left(\frac{h}{2}\right)^3W_3\right)}{\partial\phi}\right)\right\}-\frac{P}{\mathcal{R}^2\,sin^2(\phi)}\frac{\partial^2\left(W_0+\left(\frac{h}{2}\right)W_1+\left(\frac{h}{2}\right)^2W_2+\left(\frac{h}{2}\right)^3W_3\right)}{\partial\theta^2}=\mathcal{G}_0\frac{\partial^2W_0}{\partial t^2}+\mathcal{G}_1\frac{\partial^2W_1}{\partial t^2}+\mathcal{G}_2\frac{\partial^2W_2}{\partial t^2}+\mathcal{G}_3\frac{\partial^2W_3}{\partial t^2}, \tag{15c}$$

$$\delta\mathcal{U}_1: \frac{1}{\mathcal{R}}\frac{\partial \mathfrak{m}_{\phi\phi}}{\partial\phi}+\frac{cot(\phi)}{\mathcal{R}}\left(\mathfrak{m}_{\phi\phi}-\mathfrak{m}_{\theta\theta}\right)+\frac{1}{\mathcal{R}\,sin(\phi)}\frac{\partial \mathfrak{m}_{\phi\theta}}{\partial\theta}+\frac{\mathfrak{m}_{\phi z}}{\mathcal{R}}-\mathfrak{n}_{\phi z}=\mathcal{G}_1\frac{\partial^2\mathcal{U}_0}{\partial t^2}+\mathcal{G}_2\frac{\partial^2\mathcal{U}_1}{\partial t^2}+\mathcal{G}_3\frac{\partial^2\mathcal{U}_2}{\partial t^2}+\mathcal{G}_4\frac{\partial^2\mathcal{U}_3}{\partial t^2}, \tag{15d}$$

$$\delta\mathcal{V}_1: \frac{1}{\mathcal{R}\,sin(\phi)}\frac{\partial \mathfrak{m}_{\theta\theta}}{\partial\theta}+\frac{1}{\mathcal{R}}\frac{\partial \mathfrak{m}_{\phi\theta}}{\partial\phi}+\frac{2\,cot(\phi)}{\mathcal{R}}\mathfrak{m}_{\phi\theta}+\frac{\mathfrak{m}_{\theta z}}{\mathcal{R}}-\mathfrak{n}_{\theta z}=\mathcal{G}_1\frac{\partial^2\mathcal{V}_0}{\partial t^2}+\mathcal{G}_2\frac{\partial^2\mathcal{V}_1}{\partial t^2}+\mathcal{G}_3\frac{\partial^2\mathcal{V}_2}{\partial t^2}+\mathcal{G}_4\frac{\partial^2\mathcal{V}_3}{\partial t^2}, \tag{15e}$$

$$\delta\mathcal{W}_1: \frac{1}{\mathcal{R}}\frac{\partial \mathfrak{m}_{\phi z}}{\partial\phi}+\frac{1}{\mathcal{R}\,sin(\phi)}\frac{\partial \mathfrak{m}_{\theta z}}{\partial\theta}+\frac{cot(\phi)}{\mathcal{R}}\mathfrak{m}_{\phi z}-\frac{\mathfrak{m}_{\phi\phi}+\mathfrak{m}_{\theta\theta}}{\mathcal{R}}-\mathfrak{n}_{zz}+\left(\frac{h}{2}\right)\times\left(-\left\{\frac{P}{\mathcal{R}^2\,sin(\phi)}\frac{\partial}{\partial\phi}\left(sin(\phi)\frac{\partial\left(W_0+\left(\frac{h}{2}\right)W_1+\left(\frac{h}{2}\right)^2W_2+\left(\frac{h}{2}\right)^3W_3\right)}{\partial\phi}\right)\right\}-\frac{P}{\mathcal{R}^2\,sin^2(\phi)}\frac{\partial^2\left(W_0+\left(\frac{h}{2}\right)W_1+\left(\frac{h}{2}\right)^2W_2+\left(\frac{h}{2}\right)^3W_3\right)}{\partial\theta^2}\right)=\mathcal{G}_1\frac{\partial^2W_0}{\partial t^2}+\mathcal{G}_2\frac{\partial^2W_1}{\partial t^2}+\mathcal{G}_3\frac{\partial^2W_2}{\partial t^2}+\mathcal{G}_4\frac{\partial^2W_3}{\partial t^2}, \tag{15f}$$

$$\delta\mathcal{U}_2: \frac{1}{\mathcal{R}}\frac{\partial \mathfrak{p}_{\phi\phi}}{\partial\phi}+\frac{cot(\phi)}{\mathcal{R}}\left(\mathfrak{p}_{\phi\phi}-\mathfrak{p}_{\theta\theta}\right)+\frac{1}{\mathcal{R}\,sin(\phi)}\frac{\partial \mathfrak{p}_{\phi\theta}}{\partial\theta}+\frac{\mathfrak{p}_{\phi z}}{\mathcal{R}}-2\mathfrak{m}_{\phi z}=\mathcal{G}_2\frac{\partial^2\mathcal{U}_0}{\partial t^2}+\mathcal{G}_3\frac{\partial^2\mathcal{U}_1}{\partial t^2}+\mathcal{G}_4\frac{\partial^2\mathcal{U}_2}{\partial t^2}+\mathcal{G}_5\frac{\partial^2\mathcal{U}_3}{\partial t^2}, \tag{15g}$$

$$\delta\mathcal{V}_1: \frac{1}{\mathcal{R}\,sin(\phi)}\frac{\partial \mathfrak{p}_{\theta\theta}}{\partial\theta}+\frac{1}{\mathcal{R}}\frac{\partial \mathfrak{p}_{\phi\theta}}{\partial\phi}+\frac{2\,cot(\phi)}{\mathcal{R}}\mathfrak{p}_{\phi\theta}+\frac{\mathfrak{p}_{\theta z}}{\mathcal{R}}-2\mathfrak{m}_{\theta z}=\mathcal{G}_2\frac{\partial^2\mathcal{V}_0}{\partial t^2}+\mathcal{G}_3\frac{\partial^2\mathcal{V}_1}{\partial t^2}+\mathcal{G}_4\frac{\partial^2\mathcal{V}_2}{\partial t^2}+\mathcal{G}_5\frac{\partial^2\mathcal{V}_3}{\partial t^2}, \tag{15h}$$

$$\delta\mathcal{W}_2: \frac{1}{\mathcal{R}}\frac{\partial \mathfrak{p}_{\phi z}}{\partial\phi}+\frac{1}{\mathcal{R}\,sin(\phi)}\frac{\partial \mathfrak{p}_{\theta z}}{\partial\theta}+\frac{cot(\phi)}{\mathcal{R}}\mathfrak{p}_{\phi z}-\frac{\mathfrak{p}_{\phi\phi}+\mathfrak{p}_{\theta\theta}}{\mathcal{R}}-2\mathfrak{m}_{zz}+\left(\frac{h}{2}\right)^2\times\left(-\left\{\frac{P}{\mathcal{R}^2\,sin(\phi)}\frac{\partial}{\partial\phi}\left(sin(\phi)\frac{\partial\left(W_0+\left(\frac{h}{2}\right)W_1+\left(\frac{h}{2}\right)^2W_2+\left(\frac{h}{2}\right)^3W_3\right)}{\partial\phi}\right)\right\}-\frac{P}{\mathcal{R}^2\,sin^2(\phi)}\frac{\partial^2\left(W_0+\left(\frac{h}{2}\right)W_1+\left(\frac{h}{2}\right)^2W_2+\left(\frac{h}{2}\right)^3W_3\right)}{\partial\theta^2}\right)=\mathcal{G}_2\frac{\partial^2W_0}{\partial t^2}+\mathcal{G}_3\frac{\partial^2W_1}{\partial t^2}+\mathcal{G}_4\frac{\partial^2W_2}{\partial t^2}+\mathcal{G}_5\frac{\partial^2W_3}{\partial t^2}, \tag{15i}$$

$$\delta\mathcal{U}_3: \frac{1}{\mathcal{R}}\frac{\partial \mathfrak{q}_{\phi\phi}}{\partial\phi}+\frac{cot(\phi)}{\mathcal{R}}\left(\mathfrak{q}_{\phi\phi}-\mathfrak{q}_{\theta\theta}\right)+\frac{1}{\mathcal{R}\,sin(\phi)}\frac{\partial \mathfrak{q}_{\phi\theta}}{\partial\theta}+\frac{\mathfrak{q}_{\phi z}}{\mathcal{R}}-3\mathfrak{p}_{\phi z}=\mathcal{G}_3\frac{\partial^2\mathcal{U}_0}{\partial t^2}+\mathcal{G}_4\frac{\partial^2\mathcal{U}_1}{\partial t^2}+\mathcal{G}_5\frac{\partial^2\mathcal{U}_2}{\partial t^2}+\mathcal{G}_6\frac{\partial^2\mathcal{U}_3}{\partial t^2}, \tag{15j}$$

$$\delta\mathcal{V}_3: \frac{1}{\mathcal{R}\,sin(\phi)}\frac{\partial \mathfrak{q}_{\theta\theta}}{\partial\theta}+\frac{1}{\mathcal{R}}\frac{\partial \mathfrak{q}_{\phi\theta}}{\partial\phi}+\frac{2\,cot(\phi)}{\mathcal{R}}\mathfrak{q}_{\phi\theta}+\frac{\mathfrak{q}_{\theta z}}{\mathcal{R}}-3\mathfrak{p}_{\theta z}=\mathcal{G}_3\frac{\partial^2\mathcal{V}_0}{\partial t^2}+\mathcal{G}_4\frac{\partial^2\mathcal{V}_1}{\partial t^2}+\mathcal{G}_5\frac{\partial^2\mathcal{V}_2}{\partial t^2}+\mathcal{G}_6\frac{\partial^2\mathcal{V}_3}{\partial t^2}. \tag{15k}$$

$$\delta\mathcal{W}_3: \frac{1}{\mathcal{R}}\frac{\partial \mathfrak{q}_{\phi z}}{\partial\phi}+\frac{1}{\mathcal{R}\,sin(\phi)}\frac{\partial \mathfrak{q}_{\theta z}}{\partial\theta}+\frac{cot(\phi)}{\mathcal{R}}\mathfrak{q}_{\phi z}-\frac{\mathfrak{q}_{\phi\phi}+\mathfrak{q}_{\theta\theta}}{\mathcal{R}}-3\mathfrak{p}_{zz}+\left(\frac{h}{2}\right)^3\times\left(-\left\{\frac{P}{\mathcal{R}^2\,sin(\phi)}\frac{\partial}{\partial\phi}\left(sin(\phi)\frac{\partial\left(W_0+\left(\frac{h}{2}\right)W_1+\left(\frac{h}{2}\right)^2W_2+\left(\frac{h}{2}\right)^3W_3\right)}{\partial\phi}\right)\right\}-\frac{P}{\mathcal{R}^2\,sin^2(\phi)}\frac{\partial^2\left(W_0+\left(\frac{h}{2}\right)W_1+\left(\frac{h}{2}\right)^2W_2+\left(\frac{h}{2}\right)^3W_3\right)}{\partial\theta^2}\right)=\mathcal{G}_3\frac{\partial^2W_0}{\partial t^2}+\mathcal{G}_4\frac{\partial^2W_1}{\partial t^2}+\mathcal{G}_5\frac{\partial^2W_2}{\partial t^2}+\mathcal{G}_6\frac{\partial^2W_3}{\partial t^2}, \tag{15l}$$

The mechanical boundary conditions are defined as:

$$\delta\mathcal{U}_0: n_\phi\frac{\mathfrak{n}_{\phi\phi}}{\mathcal{R}}+n_\theta\frac{\mathfrak{n}_{\phi\theta}}{\mathcal{R}\,sin(\phi)}=n_\phi\bar{\mathfrak{n}}_{\phi\phi}+n_\theta\bar{\mathfrak{n}}_{\phi\theta}, \tag{16a}$$

$$\delta\mathcal{V}_0: n_\phi\frac{\mathfrak{n}_{\phi\theta}}{\mathcal{R}}+n_\theta\frac{\mathfrak{n}_{\theta\theta}}{\mathcal{R}\,sin(\phi)}=n_\phi\bar{\mathfrak{n}}_{\phi\theta}+n_\theta\bar{\mathfrak{n}}_{\theta\theta}, \tag{16b}$$

$$\delta\mathcal{W}_0: n_\phi\frac{\mathfrak{q}_{\phi z}}{\mathcal{R}}+n_\theta\frac{\mathfrak{q}_{\theta z}}{\mathcal{R}\,sin(\phi)}=n_\phi\bar{\mathfrak{n}}_{\phi z}+n_\theta\bar{\mathfrak{n}}_{\theta z}, \tag{16c}$$

$$\delta\mathcal{U}_1: n_\phi\frac{\mathfrak{m}_{\phi\phi}}{\mathcal{R}}+n_\theta\frac{\mathfrak{m}_{\phi\theta}}{\mathcal{R}\,sin(\phi)}=n_\phi\bar{\mathfrak{m}}_{\phi\phi}+n_\theta\bar{\mathfrak{m}}_{\phi\theta}, \tag{16d}$$

$$\delta\mathcal{V}_1: n_\phi\frac{\mathfrak{m}_{\phi\theta}}{\mathcal{R}}+n_\theta\frac{\mathfrak{m}_{\theta\theta}}{\mathcal{R}\,sin(\phi)}=n_\phi\bar{\mathfrak{m}}_{\phi\theta}+n_\theta\bar{\mathfrak{m}}_{\theta\theta}, \tag{16e}$$

$$\delta\mathcal{W}_1: n_\phi\frac{\mathfrak{m}_{\phi z}}{\mathcal{R}}+n_\theta\frac{\mathfrak{m}_{\theta z}}{\mathcal{R}\,sin(\phi)}=n_\phi\bar{\mathfrak{m}}_{\phi z}+n_\theta\bar{\mathfrak{m}}_{\theta z}, \tag{16f}$$

$$\delta\mathcal{U}_2: n_\phi\frac{\mathfrak{p}_{\phi\phi}}{\mathcal{R}}+n_\theta\frac{\mathfrak{p}_{\phi\theta}}{\mathcal{R}\,sin(\phi)}=n_\phi\bar{\mathfrak{p}}_{\phi\phi}+n_\theta\bar{\mathfrak{p}}_{\phi\theta}, \tag{16g}$$

$$\delta\mathcal{V}_2: n_\phi\frac{\mathfrak{p}_{\phi\theta}}{\mathcal{R}}+n_\theta\frac{\mathfrak{p}_{\theta\theta}}{\mathcal{R}\,sin(\phi)}=n_\phi\bar{\mathfrak{p}}_{\phi\theta}+n_\theta\bar{\mathfrak{p}}_{\theta\theta}, \tag{16h}$$

$$\delta\mathcal{W}_2: n_\phi\frac{\mathfrak{p}_{\phi z}}{\mathcal{R}}+n_\theta\frac{\mathfrak{p}_{\theta z}}{\mathcal{R}\,sin(\phi)}=n_\phi\bar{\mathfrak{p}}_{\phi z}+n_\theta\bar{\mathfrak{p}}_{\theta z}. \tag{16i}$$

$$\delta\mathcal{U}_3: n_\phi\frac{\mathfrak{q}_{\phi\phi}}{\mathcal{R}}+n_\theta\frac{\mathfrak{q}_{\phi\theta}}{\mathcal{R}\,sin(\phi)}=n_\phi\bar{\mathfrak{q}}_{\phi\phi}+n_\theta\bar{\mathfrak{q}}_{\phi\theta}, \tag{16j}$$

$$\delta\mathcal{V}_3: n_\phi\frac{\mathfrak{q}_{\phi\theta}}{\mathcal{R}}+n_\theta\frac{\mathfrak{q}_{\theta\theta}}{\mathcal{R}\,sin(\phi)}=n_\phi\bar{\mathfrak{q}}_{\phi\theta}+n_\theta\bar{\mathfrak{q}}_{\theta\theta}, \tag{16k}$$

$$\delta\mathcal{W}_3: n_\phi\frac{\mathfrak{q}_{\phi z}}{\mathcal{R}}+n_\theta\frac{\mathfrak{q}_{\theta z}}{\mathcal{R}\,sin(\phi)}=n_\phi\bar{\mathfrak{q}}_{\phi z}+n_\theta\bar{\mathfrak{q}}_{\theta z}. \tag{16l}$$

where (n_ϕ, n_θ) denotes the unit normal-to-boundary vector and the bar $(\bar{.})$ denotes the prescribed values of the resultants.

Where

$$\{\mathfrak{n}_{\phi\phi},\mathfrak{m}_{\phi\phi},\mathfrak{p}_{\phi\phi},\mathfrak{q}_{\phi\phi}\}=\int_{-h/2}^{h/2}\sigma_{\phi\phi}\{1,z,z^2,z^3\}\,dz, \tag{17a}$$

$$\{\mathfrak{n}_{\theta\theta},\mathfrak{m}_{\theta\theta},\mathfrak{p}_{\theta\theta},\mathfrak{q}_{\theta\theta}\}=\int_{-h/2}^{h/2}\sigma_{\theta\theta}\{1,z,z^2,z^3\}\,dz, \tag{17b}$$

$$\{\mathfrak{n}_{zz},\mathfrak{m}_{zz},\mathfrak{p}_{zz},\mathfrak{q}_{zz}\}=\int_{-h/2}^{h/2}\sigma_{zz}\{1,z,z^2,z^3\}\,dz, \tag{17c}$$

$$\{\mathfrak{n}_{\phi\theta}, \mathfrak{m}_{\phi\theta}, \mathfrak{p}_{\phi\theta}, \mathfrak{q}_{\phi\theta}\} = \int_{-h/2}^{h/2} \sigma_{\phi\theta}\{1, z, z^2, z^3\}\, dz, \quad (17d)$$

$$\{\mathfrak{n}_{\phi z}, \mathfrak{m}_{\phi z}, \mathfrak{p}_{\phi z}, \mathfrak{q}_{\phi z}\} = \int_{-h/2}^{h/2} \sigma_{\phi z}\{1, z, z^2, z^3\}\, dz, \quad (17e)$$

$$\{\mathfrak{n}_{\theta z}, \mathfrak{m}_{\theta z}, \mathfrak{p}_{\theta z}, \mathfrak{q}_{\theta z}\} = \int_{-h/2}^{h/2} \sigma_{\theta z}\{1, z, z^2, z^3\}\, dz, \quad (17f)$$

$$\mathcal{G}_i = \int_{-h/2}^{h/2} \rho z^i dz. \quad i = 1,2,3,4,5,6 \quad (17g)$$

4. Solution procedure

The Hyperbolic Differential Quadrature Method (HDQM) is a powerful numerical technique that has gained significant attention in engineering applications due to its efficiency and accuracy in solving complex boundary value problems, particularly those involving wave propagation and hyperbolic partial differential equations. This method is based on the Differential Quadrature Method (DQM), which approximates the derivatives of a function using weighted sums of function values at discrete points. The hyperbolic form of the method is particularly suitable for problems that involve wave-like phenomena, such as vibrations, acoustics, and fluid dynamics. In engineering, the HDQM provides an invaluable tool for solving a wide variety of problems in structural dynamics, heat transfer, and fluid mechanics. The method's ability to handle complex geometries and boundary conditions makes it ideal for real-world applications, such as smart structures, seismic analysis, and aerospace engineering. It enables engineers to model and analyze systems with time-dependent behavior, offering insights into dynamic responses and stability under different loading conditions. The HDQM can handle complex systems with higher-order derivatives, making it particularly useful for analyzing systems that involve higher-dimensional wave propagation, such as Lamb waves in composite materials or acoustic waves in structural materials. One of the key advantages of the HDQM is its ability to deliver high accuracy with fewer grid points, compared to traditional numerical methods like finite difference or finite element methods. This is especially important in problems where computational resources are limited or when dealing with large-scale systems, as it reduces both computational cost and memory usage. The method's high accuracy makes it ideal for engineering simulations that require precise results over long time periods or large domains, such as predicting the effects of thermal shock, impact, or vibration. Additionally, HDQM is highly flexible and can be applied to a wide range of engineering disciplines, from civil engineering to mechanical engineering and electrical engineering. By providing a robust tool for solving wave-based problems, it helps engineers design safer and more efficient structures and systems, improving performance, reliability, and sustainability. The method's ability to incorporate complex material properties, boundary conditions, and multi-physics interactions makes it a versatile and powerful tool for modern engineering challenges, driving innovations in structural design, damage detection, and energy harvesting. Based on the approaches, the estimated pth derivative connected to a function $f(\phi)$ is:

$$\frac{\partial^p f(\phi)}{\partial \phi^p} = \sum_{j=1}^{N_\phi} \mathbb{A}_{ij}^{(p)} f(\phi)\ for\ i = 1,2,\ldots,N_\phi \quad (18)$$

In this context, N represents the selection of discrete points from the solution field. For the ith point in the solution domain, $\mathbb{A}_{ij}^{(p)}$ corresponds to the weighting coefficients ($j = 1,2,\ldots,N_\phi$). This method approximates a partial differential equation by converting it into a system of algebraic equations. As evident from Eq. (18), determining the weighting coefficients plays a pivotal role in both the DQ and HDQ methods. The following examples illustrate the specific steps involved in calculating the weighting coefficients for each approach.

4.1 Differential quadrature method

The weighting coefficients $\mathbb{A}_{ij}^{(p)}$ can be determined using the recurrence formula of the DQ method, as given by:

$$\mathbb{A}_{ij}^{(p)} = n\left(\mathbb{A}_{ii}^{(p-1)}\mathbb{A}_{ij}^{(1)} - \frac{\mathbb{A}_{ij}^{(p-1)}}{\phi_i - \phi_j}\right), \quad p = 2,3,\ldots,N_\phi - 1\ \ and\ \ i,j = 1,2,\ldots,N_\phi, \quad (19)$$

Herein, $\mathbb{A}_{ij}^{(1)}$ can be determined:

$$\mathbb{A}_{ij}^{(1)} = \frac{M^{(1)}(\phi_i)}{(\phi_i - \phi_j)M^{(1)}(\phi_j)}, i,j = 1,2,\ldots,N_\phi \quad (20)$$

When $i = j$, the corresponding weighting coefficients are as follows:

$$\mathbb{A}_{ii}^{(p)} = -\sum_{j=1,j\neq i}^{N_\phi} \mathbb{A}_{ij}^{(p)},\ i = 2,3,\ldots,N_\phi\ \ and\ \ p = 1,2,\ldots,N_\phi - 1, \quad (21)$$

In Eq. (20), $M^{(1)}$ can be formulated by:

$$M^{(1)}(\phi_k) = -\sum_{j=1,j\neq k}^{N_\phi} (\phi_k - \phi_j),\ \ for\ \ k = 1,2,3,\ldots,N_\phi \quad (22)$$

4.2 Harmonic Differential Quadrature Method (HDQM)

For $i \neq j$, the following formula yields the appropriate weights for the first-order derivatives $\mathbb{A}_{ij}^{(1)}$:

$$\mathbb{A}_{ij}^{(1)} = \frac{\pi P(\phi_i)}{2P(\phi_j)\sin\left[\frac{(\phi_i - \phi_j)}{2\pi}\right]}, \quad i,j = 1,2,\ldots,N_\phi \quad (23)$$

Herein,

$$P(\phi_i) = -\sum_{j=1,j\neq i}^{N_\phi} \sin\left(\frac{\pi(\phi_i - \phi_j)}{2}\right), for\ j = 1,2,3,\ldots,N_\phi \quad (24)$$

The 1st order derivatives $\mathbb{A}_{ij}^{(1)}$ for $i = j$ have weights defined as:

$$\mathbb{A}_{ii}^{(1)} = -\sum_{j=1, j\neq i}^{N_\phi} \mathbb{A}_{ij}^{(1)}, for\ i = 1,2,3,\ldots,N_\phi \quad (25)$$

Second-order derivative weights $\mathbb{A}_{ij}^{(2)}$ for $i \neq j$ may be calculated by:

$$\mathbb{A}_{ij}^{(2)} = \mathbb{A}_{ij}^{(1)}\left(2\mathbb{A}_{ij}^{(1)} - \pi ctg\left(\frac{\phi_i - \phi_j}{2} \times \pi\right)\right), i, j = 1,2,3,\ldots,N_\phi. \quad (26)$$

For $i = j$, the derivatives $\mathbb{A}_{ij}^{(2)}$'s weighting factors are as follows:

$$\mathbb{A}_{ii}^{(2)} = -\sum_{j=1, j\neq i}^{N_\phi} \mathbb{A}_{ij}^{(2)}, for\ i = 1,2,3,\ldots,N_\phi \quad (27)$$

4.3 Two-dimensional approximation

The HDQ and DQ methods, initially developed for one-dimensional problems, can be straightforwardly extended to three-dimensional approximations. The formulas for approximating a two-dimensional unknown function $f\ (\phi, \theta)$ are provided below:

$$\left.\frac{\partial f}{\partial \phi}\right|_{\phi=\phi_i,\theta=\theta_j} = \sum_{p=1}^{N_\phi}\sum_{k=1}^{N_\theta} \mathbb{A}_{ip}^{\phi} I_{pk}^{\theta} f_{kj}, \quad (28a)$$

$$\left.\frac{\partial f}{\partial \theta}\right|_{\phi=\phi_i,\theta=\theta_j} = \sum_{p=1}^{N_\phi}\sum_{k=1}^{N_\theta} I_{ip}^{\phi} \mathbb{A}_{pk}^{\theta} f_{kj}, \quad (28b)$$

$$\frac{\partial}{\partial \phi}\left(\left.\frac{\partial f}{\partial \theta}\right|_{\phi=\phi_i,\theta=\theta_j}\right) = \sum_{p=1}^{N_\phi}\sum_{k=1}^{N_\theta} \mathbb{A}_{ip}^{\phi} \mathbb{A}_{pk}^{\theta} f_{kj}, \quad (28c)$$

$$\left.\frac{\partial^2 f}{\partial \phi^2}\right|_{\phi=\phi_i,\theta=\theta_j} = \sum_{p=1}^{N_\phi}\sum_{k=1}^{N_\theta} \mathbb{B}_{ip}^{\phi} I_{pk}^{\theta} f_{kj}, \quad (28d)$$

$$\left.\frac{\partial^2 f}{\partial \theta^2}\right|_{\phi=\phi_i,\theta=\theta_j} = \sum_{p=1}^{N_\phi}\sum_{k=1}^{N_\theta} I_{ip}^{\phi} \mathbb{B}_{pk}^{\theta} f_{kj}. \quad (28e)$$

Here, $\mathbb{A}_{ip}^{\phi}$, $\mathbb{A}_{pk}^{\theta}$, $\mathbb{B}_{ip}^{\phi}$, and $\mathbb{B}_{pk}^{\theta}$ represent the weighting coefficients for the *p*th partial derivatives of the function at the point (i, j) with respect to the ϕ and θ axes. N_ϕ and N_θ denote the total number of discrete points selected along the r, and directions, respectively. The parameters I_{ip}^{ϕ}, I_{pk}^{θ}, I_{ip}^{ϕ}, and I_{pk}^{θ} refer to the identity matrix. Similarly, the Chebyshev–Gauss–Lobatto grid distribution can be considered, where the coordinates of the grid points (ϕ_i, θ_j) on the reference surface can be determined by:

$$\phi_i = \phi_0 + \frac{\varphi}{2}\left(1 - cos\left(\frac{(i-1)}{(N_\phi - 1)}\pi\right)\right) i = 1,2,3,\ldots,N_\phi, \quad (29a)$$

$$\theta_j = \frac{\beta}{2}\left(1 - cos\left(\frac{(j-1)}{(N_\theta - 1)}\pi\right)\right) j = 1,2,3,\ldots,N_\theta, \quad (29b)$$

The displacement field of the functionally graded composite nanostructured thick spherical shell is obtained using the method of variable separation, which can be expressed as:

$$\mathcal{U}_J(\phi, \theta, t) = \mathbb{u}_J(\phi, \theta)e^{i\omega t}, \quad (30a)$$

$$\mathcal{V}_J(\phi, \theta, t) = \mathbb{v}_J(\phi, \theta)e^{i\omega t}, \quad (30b)$$

$$\mathcal{W}_J(\phi, \theta, t) = \mathbb{w}_J(\phi, \theta)e^{i\omega t}. \quad (30c)$$

where $J = 0,1,2,3$. Also, i is the imaginary unit $\left(i = \sqrt{-1}\right)$. By substituting Eqs. (17a-g), (28a-e), (30a-c), into Eqs. (15a-l), and (16a-l), yields the following:

$$(-\omega^2[\mathbb{M}] + [\mathbb{K}])\{\bar{\mathbb{X}}\} = 0, \quad (31a)$$

$$\{\bar{\mathbb{X}}\} = \{\mathbb{u}_0\ \mathbb{v}_0\ \mathbb{w}_0\ \mathbb{u}_1\ \mathbb{v}_1\ \mathbb{w}_1\ \mathbb{u}_2\ \mathbb{v}_2\ \mathbb{w}_2\ \mathbb{u}_3\ \mathbb{v}_3\ \mathbb{w}_3\}^T. \quad (31b)$$

In the given equations, '$\mathbb{M}$', and '$\mathbb{K}$' represent the mass and stiffness matrices, respectively. The solution to Eq. (31a) provides the natural frequencies of the system.

5. Results and discussion

5.1 Verification study

Table 1 compares the frequency results for an isotropic spherical shell under two different boundary conditions: Free-Free and Clamp-Clamp. It shows the results for different mode numbers (0 to 4), comparing the present findings with those from the referenced study (Ref. (Tornabene, Viscoti, Dimitri, *et al*. 2021)). For each mode number, the table provides the frequencies under both boundary conditions. In the Free-Free condition, the frequencies for Mode 0, 1, 2, 3, and 4 are 0.8700, 0.8635, 0.0568, 0.1528, and 0.27982, respectively. In comparison, the reference study reports slightly different values for these modes: 0.8705, 0.8641, 0.0573, 0.1532, and 0.2790. For the Clamp-Clamp condition, the frequencies are slightly higher for all modes. The corresponding values for the present study are 0.9862, 1.0260, 1.0024, 0.9973, and 1.0420, compared to 0.9871, 1.0264, 1.0029, 0.9980, and 1.0427 in the reference study. These comparisons show the consistency of the present study's results with the reference values, suggesting that the methodology used to calculate the frequencies for the spherical shell's modes is accurate and reliable.

5.2 Parametric results

Fig. 3 demonstrates the effect of varying the shell's angle on the natural frequencies of spherical shells made of functionally graded carbon nanotube-reinforced composites. The plot shows natural frequency as a function of the shell's radius. It can be observed that the natural frequency decreases as the shell's angle increases from ϕ_0= 10° to ϕ_0= 40°, with larger values of ϕ_0 leading to lower natural frequencies at any given radius. This suggests that higher concentrations of carbon nanotubes influence the material properties, specifically stiffness, of the FG-CNTRC shells,

Table 1 Comparison of frequency results for the isotropic spherical shell

Mode Number	Free-Free		Clamp-Clamp	
	Present	Ref. (Tornabene *et al*. 2021)	Present	Ref. (Tornabene *et al*. 2021)
0	0.8700	0.8705	0.9862	0.9871
1	0.8635	0.8641	1.0260	1.0264
2	0.0568	0.0573	1.0024	1.0029
3	0.1528	0.1532	0.9973	0.9980
4	0.27982	0.2790	1.0420	1.0427

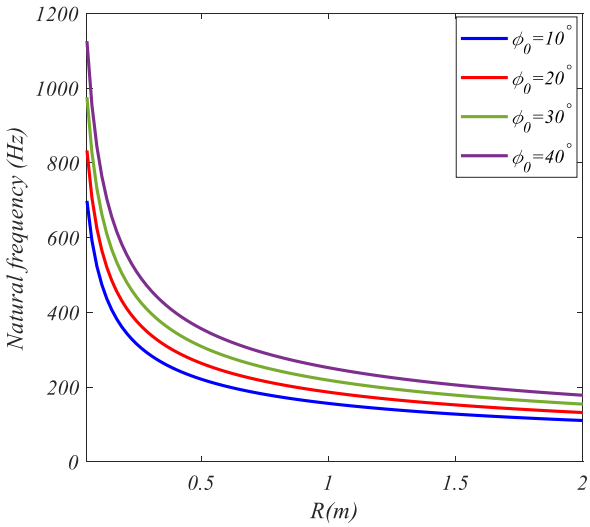

Fig. 3 The effect of varying the shell's angle on the natural frequencies of spherical shells made of functionally graded carbon nanotube-reinforced composites

thus modifying the shell's vibrational characteristics. As the radius increases, the natural frequency decreases, which is consistent with the expected behavior for thin-walled spherical shells, where the frequency is inversely proportional to the structural dimensions. The findings indicate that increasing the shell's angle generally reduces the natural frequency, highlighting the role of structure distribution in tuning the vibrational response of the shell.

Fig. 4 illustrates the impact of the weight fraction of carbon nanotubes on the natural frequencies of the FG-CNTRC spherical shell. The weight fraction is varied from 0% to 15%, and the natural frequency is plotted as a function of the shell's radius. The results indicate a clear trend where increasing the weight fraction of carbon nanotubes leads to a significant reduction in the natural frequency at any given radius. This trend is attributed to the enhanced stiffness imparted by the carbon nanotubes in the composite material. As the radius of the shell increases, the natural frequency decreases for all values of W_{CNT}, reflecting the typical behavior of spherical shells under vibrational loading. The plots for different W_{CNT} values suggest that the carbon nanotube reinforcement provides a stiffer material matrix, which ultimately influences the dynamic characteristics of the shell. This finding underscores the importance of selecting an optimal weight fraction to balance mechanical performance and dynamic

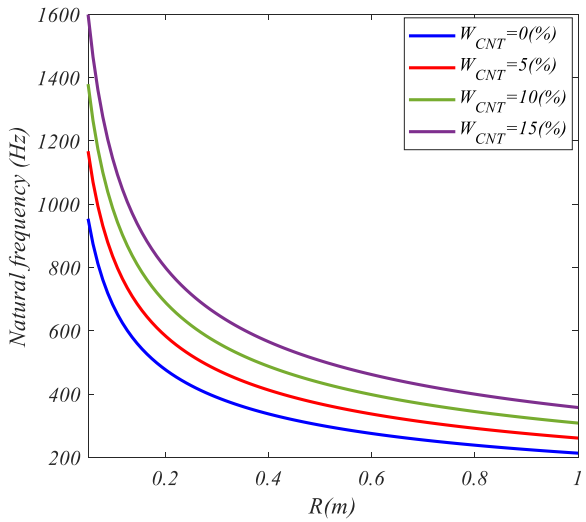

Fig. 4 The impact of the weight fraction of carbon nanotubes on the natural frequencies of the FG-CNTRC spherical shell

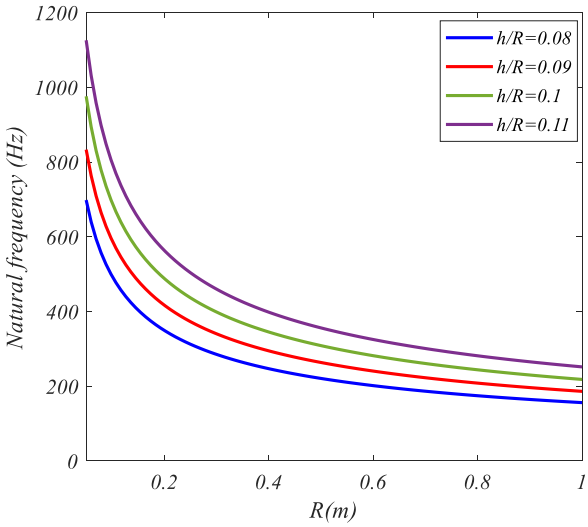

Fig. 5 The effect of the shell's thickness-to-radius ratio on its natural frequency

behavior in FG-CNTRC shell designs.

Fig. 5 investigates the effect of the shell's thickness-to-radius ratio ($h/\mathcal{R}$) on its natural frequency. Four different values of the thickness-to-radius ratio, ranging from $h/\mathcal{R}$ = 0.08 to $h/\mathcal{R}$ = 0.11, are considered. The plot shows that as the thickness-to-radius ratio increases, the natural frequency decreases. This is a typical trend observed in shell dynamics, where thinner shells exhibit higher natural frequencies due to their reduced mass and greater flexibility. Conversely, thicker shells tend to have lower natural frequencies because of their higher mass and stiffness. The curves for different $h/\mathcal{R}$ ratios clearly illustrate that increasing the thickness-to-radius ratio leads to a reduction in the natural frequency for all values of $\mathcal{R}$. This relationship highlights the importance of shell geometry in influencing the vibrational response and stability of the structure. Designers of FG-CNTRC spherical shells must carefully consider the $h/\mathcal{R}$ ratio to achieve desired

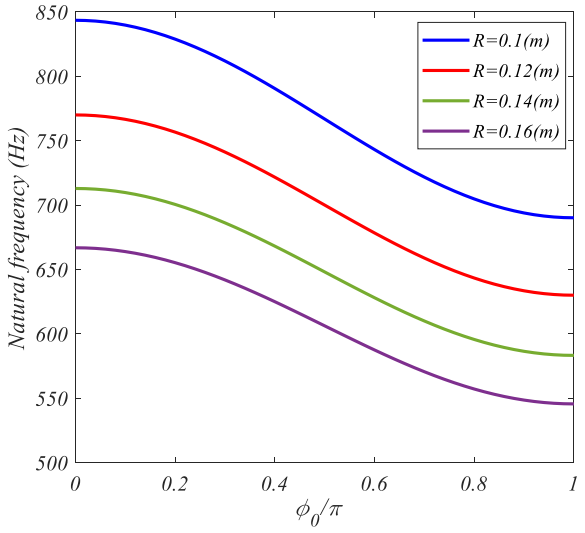

Fig. 6 The relationship between the natural frequency of a functionally graded carbon nanotube-reinforced composite spherical shell and the angular coordinate for different radii of the shell

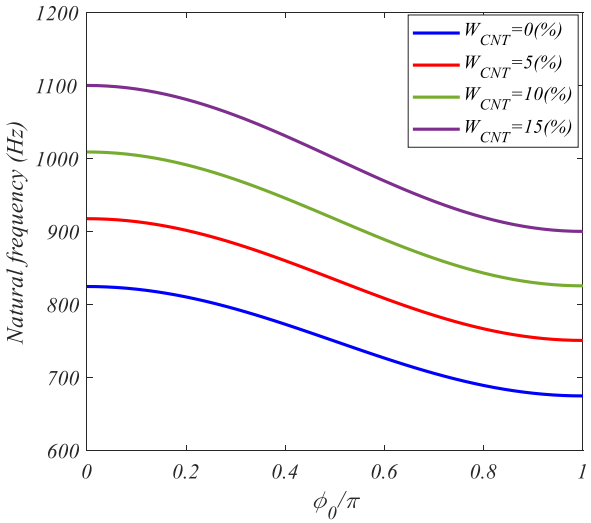

Fig. 7 The variation of natural frequency as a function of the volume fraction of carbon nanotubes, ranging from 0% to 15%, for different values of the angular coordinate

dynamic properties and avoid resonance frequencies that could affect structural integrity or performance.

Fig. 6 presents the relationship between the natural frequency of a functionally graded carbon nanotube-reinforced composite spherical shell and the angular coordinate for different radii of the shell. The radii vary from $0.1\,m$ to $0.16\,m$, with the natural frequency oscillating as a function of ϕ_0/π. The trend observed shows that for larger radii ($\mathcal{R} = 0.16\,m$), the natural frequency is lower compared to smaller radii, as expected in shell dynamics. This decrease in frequency with radius is a common feature for thin-walled spherical shells. The oscillating behavior of the natural frequency with respect to ϕ_0/π indicates that the shell's dynamic characteristics are highly sensitive to its geometric configuration conditions.

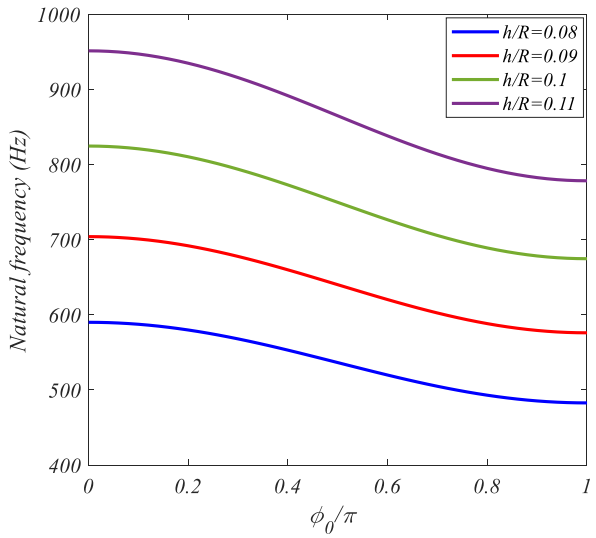

Fig. 8 The effect of the thickness-to-radius ratio on the natural frequency of the FG-CNTRC spherical shell

This plot demonstrates the interaction between shell geometry and its vibrational response, emphasizing the need for tailored design based on radius to optimize performance.

Fig. 7 shows the variation of natural frequency as a function of the volume fraction of carbon nanotubes (W_{CNT}), ranging from 0% to 15%, for different values of the angular coordinate (ϕ_0/π). The natural frequency increases as the volume fraction of carbon nanotubes increases, with the highest frequency observed at W_{CNT} = 15%. This result suggests that higher concentrations of carbon nanotubes enhance the stiffness of the FG-CNTRC shell, leading to higher natural frequencies. As the angular position (ϕ_0/π) changes, the natural frequency oscillates, reflecting the complex interaction between the carbon nanotube distribution and the shell's geometrical and boundary properties. For all values of W_{CNT}, the frequency exhibits a periodic behavior, highlighting the importance of material composition in tuning the vibrational characteristics of the structure. This plot underscores the role of ϕ_0/π in decreasing the natural frequency of spherical shells, and its potential for design optimization in engineering applications.

Fig. 8 illustrates the effect of the thickness-to-radius ratio ($h/\mathcal{R}$) on the natural frequency of the FG-CNTRC spherical shell. The ratio $h/\mathcal{R}$ is varied from 0.08 to 0.11, and the natural frequency is plotted against the angular coordinate. As the thickness-to-radius ratio increases, the natural frequency decreases. This relationship is typical for spherical shells, where thicker shells tend to have lower natural frequencies due to their increased mass and stiffness. The oscillating behavior of the natural frequency with respect to ϕ_0/π is evident, indicating that the frequency depends on the angular position of the shell. Thicker shells ($h/\mathcal{R}$ = 0.11) exhibit lower natural frequencies compared to thinner ones ($h/\mathcal{R}$ = 0.08), demonstrating that shell geometry is a crucial factor in determining the dynamic response. The periodic behavior across the angular coordinate shows that the design of

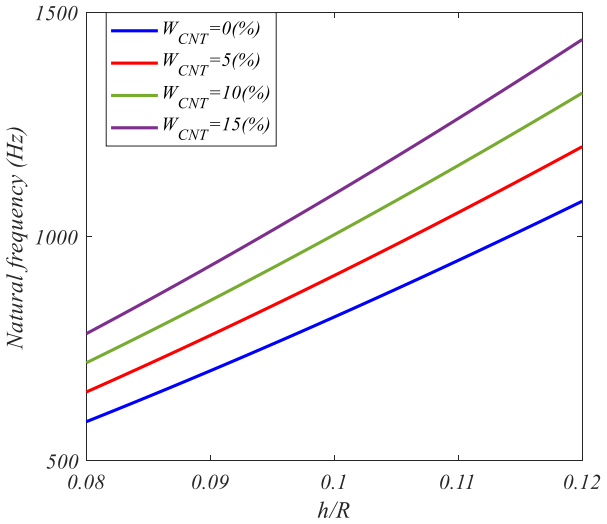

Fig. 9 The effect of varying the weight fraction of carbon nanotubes ($\boldsymbol{W_{CNT}}$) on the natural frequency of a spherical shell made of functionally graded carbon nanotube-reinforced composite

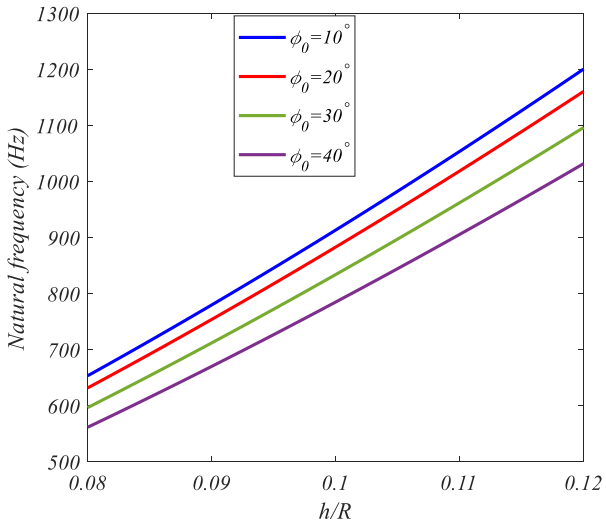

Fig. 10 shows the relationship between the natural frequency and the thickness-to-radius ratio ($\boldsymbol{h/\mathcal{R}}$) for various values of $\boldsymbol{\phi_0}$ parameter

spherical shells must consider both geometric and material factors to optimize dynamic stability and performance.

Fig. 9 demonstrates the effect of varying the weight fraction of carbon nanotubes (W_{CNT}) on the natural frequency of a spherical shell made of functionally graded carbon nanotube-reinforced composite. The weight fraction ranges from 0% to 15%, and the natural frequency is plotted against the thickness-to-radius ratio ($h/\mathcal{R}$), varying from 0.08 to 0.12. As the weight fraction of carbon nanotubes increases, the natural frequency also increases, with the curve for W_{CNT} = 15% exhibiting the highest frequency. This indicates that carbon nanotubes improve the stiffness of the material, resulting in higher natural frequencies. The linear trend for all W_{CNT} values suggest that the natural frequency increases proportionally with the thickness-to-radius ratio, which is typical of shell dynamics where

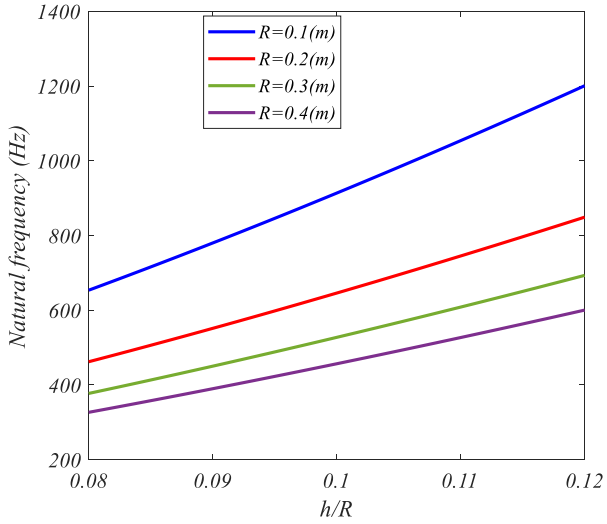

Fig. 11 The effect of radius on the natural frequency of the spherical shell as a function of the thickness-to-radius ratio

increased shell thickness enhances stiffness. The results highlight the significant role of carbon nanotube reinforcement in tuning the dynamic behavior of spherical shells, particularly in improving their vibrational characteristics through material composition.

Fig. 10 shows the relationship between the natural frequency and the thickness-to-radius ratio ($h/\mathcal{R}$) for various values of ϕ_0, ranging from 10° to 40°. As the thickness-to-radius ratio increases, the natural frequency increases for all values of ϕ_0. The natural frequency increases more rapidly with higher ϕ_0 values, with ϕ_0 = 40° exhibiting the steepest slope. This suggests that higher carbon nanotube concentrations contribute significantly to increasing the shell's stiffness, which in turn raises the natural frequency. The overall trend indicates that the vibrational characteristics of the spherical shell are heavily influenced by both the geometric configuration ($h/\mathcal{R}$) and the volume fraction of carbon nanotubes. The data emphasize the role of carbon nanotube reinforcement in enhancing the mechanical properties of the shell, making it possible to tailor the shell's dynamic response through optimal design choices.

Fig. 11 examines the effect of radius on the natural frequency of the spherical shell as a function of the thickness-to-radius ratio ($h/\mathcal{R}$). The radius is varied from 0.1 m to 0.4 m, and the natural frequency increases with the thickness-to-radius ratio for all radii. The natural frequency is higher for smaller radii, with $\mathcal{R} = 0.1\,m$ showing the highest frequency for each value of $h/\mathcal{R}$. This is in line with the general behavior of spherical shells, where smaller structures tend to have higher natural frequencies due to their reduced mass and more pronounced stiffness. As the radius increases, the natural frequency decreases, showing a typical inverse relationship between shell size and its vibrational response. The plot underscores the importance of geometric parameters such as radius and thickness-to-radius ratio in shaping the dynamic properties of the FG-CNTRC spherical shells, highlighting the need for careful design considerations.

6. Conclusions

In this study, we have presented a detailed analysis of the stability and design of spherical shells reinforced with functionally graded carbon nanotube-reinforced composites. By utilizing higher-order theories, we have enhanced the accuracy of the kinematic modeling, particularly through the use of the 12-variable displacement field. The Rule of Mixtures has been applied to model the material properties, allowing for an effective representation of the distribution of carbon nanotubes in the composite matrix. We have derived the governing equations using Hamilton's principle, considering both material and geometric linearity, and have solved these equations using a numerical approach based on Chebyshev–Gauss–Lobatto grid points. This method has proven efficient in providing accurate solutions, ensuring the reliability of the stability analysis. The results have revealed the significant influence of key parameters, such as the volume fraction of carbon nanotubes, on the buckling load and deformation characteristics of the spherical shells. By comparing our findings with those from previous studies, we have demonstrated a notable improvement in the accuracy of the predicted critical buckling loads and overall stability behavior. This improvement can be attributed to the higher-order theories and the refined numerical method employed in this work. This research has contributed to the growing body of knowledge in the field of nanocomposites, particularly in the design and optimization of advanced materials for structural applications. The enhanced accuracy of the stability predictions has provided valuable insights into the potential of FG-CNTRC spherical shells in engineering applications where both strength and lightweight properties are crucial. In conclusion, we have established a robust and reliable framework for the analysis and design of FG-CNTRC-reinforced spherical shells, which can be utilized for future research and development in nanostructure-based engineering materials.

References

Al-Houri, S., Al-Osta, M.A., Gawah, Q., Bourada, F., Tounsi, A., Al-Dulaijan, S.U. and Tounsi, A. (2024a), "Wave propagation analysis of composite beams reinforced with nonlinear fg-cnt distributions supported on kerr elastic foundation utilizing an improved integral first-order shear deformation theory", *Geomech. Eng.*, **39**(5), 483. https://doi.org/10.12989/gae.2024.39.5.483

Al-Houri, S., Al-Osta, M.A., Bourada, F., Gawah, Q., Tounsi, A. and Al-Dulaijan, S.U. (2024b), "Analysis of porosity-dependent wave propagation in fg-cntrc beams utilizing an integral higher-order shear deformation theory", *Int. J. Struct. Stabil. Dyn.*, 2550233. https://doi.org/10.1142/S0219455425502335

Alsubaie, A.M., Alfaqih, I., Al-Osta, M.A., Tounsi, A., Chikh, A., Mudhaffar, I.M. and Tahir, S. (2023), "Porosity-dependent vibration investigation of functionally graded carbon nanotube-reinforced composite beam", *Comput. Concr.*, **32**(1), 75-85. https://doi.org/10.12989/cac.2023.32.1.075

Alsubaie, A.M., Al-Osta, M.A., Alfaqih, I., Tounsi, A., Chikh, A., Mudhaffar, I.M., Al-Dulaijan, S.U. and Tahir, S. (2024), "Influences of porosity distributions on bending and buckling behaviour of functionally graded carbon nanotube-reinforced composite beam", *Comput. Concr.*, **34**(2), 179-193. https://doi.org/10.12989/cac.2024.34.2.179

Avcar, M., Hadji, L. and Civalek, O. (2023), "The influence of non-linear carbon nanotube reinforcement on the natural frequencies of composite beams", *Adv. Nano Res.*, **14**(5), 421-433. https://doi.org/10.12989/anr.2023.14.5.421

Ayache, B., Bennai, R., Fahsi, B., Fourn, H., Atmane, H.A. and Tounsi, A. (2018), "Analysis of wave propagation and free vibration of functionally graded porous material beam with a novel four variable refined theory", *Earthq. Struct.*, **15**(4), 369. https://doi.org/10.12989/eas.2018.15.4.369

Beitollahi, A., Janghorban, M., Bazargan-Lari, Y. and Tounsi, A. (2025), "On the variable length scale parameter for agglomeration of nanoparticles in nanocomposites", *Proceedings of the Institution of Mechanical Engineers, Part C: Journal of Mechanical Engineering Science*. https://doi.org/10.1177/09544062241308513

Belabed, Z., Bousahla, A.A. and Tounsi, A. (2024), "Vibrational and elastic stability responses of functionally graded carbon nanotube reinforced nanocomposite beams via a new quasi-3d finite element model", *Comput. Concr.*, **34**(5), 625-648. https://doi.org/10.12989/cac.2024.34.5.625

Bie, Y., Ren, H., Bui, T.Q., Madenci, E., Rabczuk, T. and Wei, Y. (2024), "Dual-horizon peridynamics modeling of coupled chemo-mechanical-damage for interface oxidation-induced cracking in thermal barrier coatings", *Comput. Meth. Appl. Mech. Eng.*, **430**, 117225. https://doi.org/10.1016/j.cma.2024.117225

Bousmaha, K., Belalia, S.A., Chorfi, S.M., Tounsi, A., Al-Osta, M.A. and Alluqmani, A.E. (2025), "On the dynamic behavior of plates made of porous advanced materials reinforced with carbon nanotubes using ap-version of finite element method", *Mech. Based Des. Struct.*, 1-30. https://doi.org/10.1080/15397734.2025.2534679

Djebbour, K. D., Nebab, M., Avcar, M., Ait Atmane, H., Bernard, F., Bennai, R. and Ikinci, B. (2025), "Stability and vibration analysis of shear deformable fg-cntrc beams resting on elastic foundations", *Adv. Nano Res.*, **18**(3), 205-221. https://doi.org/10.12989/anr.2025.18.3.205

Gawah, Q., Bourada, F., Al-Osta, M.A., Tahir, S.I., Tounsi, A. and Yaylacı, M. (2024), "An improved first-order shear deformation theory for wave propagation analysis in fg-cntrc beams resting on a viscoelastic substrate", *Int. J. Struct. Stabil. Dyn.*, **25**(1), 2550010. https://doi.org/10.1142/S0219455425500105

Gawah, Q., Al-Osta, M.A., Abdullah, M.A., Bourada, F., Tounsi, A., Ahmad, S., Al-Dulaijan, S.U. and Al-Zahrani, M.M. (2025a), "Wave propagation analysis of graphene platelet-reinforced functionally graded porous plates resting on viscoelastic foundations using an integral hsdt", *Thin Wall. Struct.*, **215**, 113502. https://doi.org/10.1016/j.tws.2025.113502

Gawah, Q., Abdullah, M.A., Al-Osta, M.A., Bourada, F., Tounsi, A., Tounsi, A. and Yaylaci, M. (2025b), "Free vibration analysis of nonlinearly dispersed fg-cntrc beams on kerr substrate using an improved fsdt", *Struct. Eng. Mech.*, **93**(6), 475-493. https://doi.org/10.12989/sem.2025.93.6.475

Guo, H., Zhuang, X. and Rabczuk, T. (2021), "A deep collocation method for the bending analysis of kirchhoff plate", *arXiv preprint*. https://doi.org/10.48550/arXiv.2102.02617

Hajmohammad, M.H., Zarei, M.S., Farrokhian, A. and Kolahchi, R. (2018), "A layerwise theory for buckling analysis of truncated conical shells reinforced by cnts and carbon fibers integrated with piezoelectric layers in hygrothermal environment", *Adv. Nano Res.*, **6**(4), 299. https://doi.org/10.12989/anr.2018.6.4.299

Khalili, S.M.R., Tafazoli, S. and Malekzadeh Fard, K. (2011), "Free vibrations of laminated composite shells with uniformly distributed attached mass using higher order shell theory including stiffness effect", *J. Sound Vib.*, **330**(26), 6355-6371. https://doi.org/10.1016/j.jsv.2011.07.004

Kumar, Y., Gupta, A. and Tounsi, A. (2021), "Size-dependent vibration response of porous graded nanostructure with fem and nonlocal continuum model", *Adv. Nano Res.*, **11**(1), 1. https://doi.org/10.12989/anr.2021.11.1.001

Liu, B., Wang, Y., Rabczuk, T., Olofsson, T. and Lu, W. (2024), "Multi-scale modeling in thermal conductivity of polyurethane incorporated with phase change materials using physics-informed neural networks", *Renew. Energy*, **220**, 119565. https://doi.org/10.1016/j.renene.2023.119565

Liu, W., Deng, L., Cai, Z., Li, D. and Rahimi, A. (2021), "Impact of in-plane follower force on the frequency response of the hybrid angle-ply laminated system via dynamic simulation and generalized differential quadrature framework", *Eng. Comput.*, 1-18. https://doi.org/10.1007/s00366-020-01215-4

SafarPour, H., Ghanbari, B. and Ghadiri, M. (2019), "Buckling and free vibration analysis of high speed rotating carbon nanotube reinforced cylindrical piezoelectric shell", *Appl. Math. Modell.*, **65**, 428-442. https://doi.org/10.1016/j.apm.2018.08.028

Safarpour, M., Rahimi, A., Alibeigloo, A., Bisheh, H. and Forooghi, A. (2021), "Parametric study of three-dimensional bending and frequency of fg-gplrc porous circular and annular plates on different boundary conditions", *Mech. Based Des. Struct.*, **49**(5), 707-737. https://doi.org/10.1080/15397734.2019.1701491

Safarpour, M. and Alibeigloo, A. (2021), "Elasticity solution for bending and frequency behavior of sandwich cylindrical shell with fg-cntrc face-sheets and polymer core under initial stresses", *Int. J. Appl. Mech.*, **13**(2), 2150020. https://doi.org/10.1142/S1758825121500204

Safarpour, M., Safarpour, H. and Civalek, O. (2025), "Wave propagation analysis of functionally graded bio-composite circular plates using an improved sinusoidal shear deformation theory resting on an advanced viscoelastic foundation", *Eur. J. Mech. A Solids*. **112**, 105688. https://doi.org/10.1016/j.euromechsol.2025.105688

Samaniego, E., Anitescu, C., Goswami, S., Nguyen-Thanh, V.M., Guo, H., Hamdia, K., Zhuang, X. and Rabczuk, T. (2020), "An energy approach to the solution of partial differential equations in computational mechanics via machine learning: concepts, implementation and applications", *Comput. Meth. Appl. Mech.*, **362**, 112790. https://doi.org/10.1016/j.cma.2019.112790

Shen, X., Li, T., Xu, L., Kiarasi, F., Babaei, M. and Asemi, K. (2024), "Free vibration analysis of fg porous spherical cap reinforced by graphene platelet resting on winkler foundation", *Adv. Nano Res.*, **16**(1), 11-26. https://doi.org/10.12989/anr.2024.16.1.011

Tornabene, F., Viscoti, M., Dimitri, R. and Aiello, M.A. (2021), "Higher order formulations for doubly-curved shell structures with a honeycomb core", *Thin Wall. Struct.*, **164**, 107789. https://doi.org/10.1016/j.tws.2021.107789

Tounsi, A., Belabed, Z., Bounouara, F., Balubaid, M., Mahmoud, S., Bousahla, A.A. and Tounsi, A. (2024), "A finite element approach for forced dynamical responses of porous fg nano-composite beams resting on viscoelastic foundations", *Int. J. Struct. Stabil. Dyn.*, 2650078. https://doi.org/10.1142/S0219455426500781

Youzera, H., Meftah, S.A., Tounsi, A., Salem, M.A., Khedher, K.M. and Yaylacı, M. (2025), "Free vibration analysis of sandwich cylindrical shells with functionally graded carbon nanotube-reinforced composite face sheets using the differential quadrature (dq) method", *Acta Mechanica*. 1-16. https://doi.org/10.1007/s00707-025-04230-y

Zerrouki, R., Zidour, M., Tounsi, A., Tounsi, A., Belabed, Z., Bousahla, A.A., Salem, M.A. and Khedher, K.M. (2024), "Buckling behavior of nonlinear fg-cnt reinforced nanocomposite beam reposed on winkler/pasternak foundation", *Comput. Concr.*, **34**(3), 297. https://doi.org/10.12989/cac.2024.34.3.297

Zhuang, X., Guo, H., Alajlan, N., Zhu, H. and Rabczuk, T. (2021), "Deep autoencoder based energy method for the bending, vibration, and buckling analysis of kirchhoff plates with transfer learning", *Eur. J. Mech. A Solids*, **87**, 104225. https://doi.org/10.1016/j.euromechsol.2021.104225

CC